PRAMANA
— journal of
physics

Vol. 64, No. 1
January 2005
pp. 95–110

Investigation of multipactor breakdown in communication satellite microwave co-axial systems

S K NAGESH[1], D REVANNASIDDIAH[2] and S V K SHASTRY[1,*]
[1]Electrical Integration Division, ISRO Satellite Centre, Airport Road, Bangalore 560 017, India
[2]Department of Physics, University of Mysore, Manasagangothri, Mysore 570 006, India
*Visiting Scientist
E-mail: sknagesh@isac.ernet.in

MS received 19 March 2004; revised 2 July 2004; accepted 27 August 2004

Abstract. Multipactor breakdown or multipactor discharge is a form of high frequency discharge that may occur in microwave components operating at very low pressures. Some RF components of multi-channel communication satellites have co-axial geometry and handle high RF power under near-vacuum conditions. The breakdown occurs due to secondary electron resonance, wherein electrons move back and forth in synchronism with the RF voltage across the gap between the inner and outer conductors of the co-axial structure. If the yield of secondary electrons from the walls of the co-axial structure is greater than unity, then the electron density increases with time and eventually leads to the breakdown. In this paper, the current due to the oscillating electrons in the co-axial geometry has been treated as a radially oriented Hertzian dipole. The electric field, due to this dipole, at any point in the coaxial structure, may then be determined by employing the dyadic Green's function technique. This field has been compared with the field that would exist in the absence of multipactor.

Keywords. Secondary electron resonance; multipactor; RF discharge.

PACS Nos 52.80.Pi; 79.20.Hx; 42.65.Ky; 84.40.Dc

1. Introduction

The multipactor breakdown or multipactor discharge represents a possible failure mechanism for spacecraft RF systems. It degrades the components, enhances system noise levels, and generates harmonics. In a co-axial geometry, the multipactor discharge (or simply, multipactor) occurs due to secondary electron resonance, wherein electrons move back and forth in synchronism with the RF voltage across the gap between the inner and outer conductors of the co-axial structure. If the yield of the secondary electrons from the walls of the co-axial structure is greater than unity, then the electron density increases with time and eventually

leads to the discharge. The occurrence of multipactor depends on pressure (less than 10^{-3} Torr), frequency, width of the RF gap, and secondary electron emission coefficient of the co-axial conductor surface material. The details of the early work on co-axial multipactor have been reported in [1–3]. A numerical approach to the estimation of electron velocities in co-axial multipactor has been described in [4].

The multipactor electrons give rise to a non-sinusoidal current and the field due to this current is of interest. The multipactor current may be modelled as a Hertzian dipole. The electric field due to this dipole, located in the space between the inner and outer conductors of the coaxial geometry, may be determined by employing the dyadic Green's function technique [5].

2. Dyadic green's function

The electromagnetic field due to a current source of density, $\bar{J}(\bar{r}')$, located at $\bar{r}'$, in the region bounded by two concentric, perfectly conducting, cylindrical structures (figure 1) may be determined by solving the following wave equations:

$$\nabla \times \nabla \times \bar{E}(\bar{r}) - k^2 \bar{E}(\bar{r}) = -j\omega\mu_0 \bar{J}(\bar{r}'), \tag{1}$$

$$\nabla \times \nabla \times \bar{H}(\bar{r}) - k^2 \bar{H}(\bar{r}) = \nabla \times \bar{J}(\bar{r}'), \tag{2}$$

where $\bar{E}(\bar{r})$ is the electric field at $\bar{r}$, $\bar{H}(\bar{r})$ is the magnetic field at $\bar{r}$, ω is the angular frequency, μ_0 is the free space permeability and

$$k = 2\pi/\lambda_0 \tag{3}$$

with λ_0 representing the wavelength.

For perfectly conducting walls, the field must satisfy the boundary condition that the tangential components of the electric field on the walls of the outer and inner conductors should be zero.

If $\bar{\bar{G}}_{\mathrm{e}}(\bar{r}, \bar{r}')$ and $\bar{\bar{G}}_{\mathrm{m}}(\bar{r}, \bar{r}')$ denote the electric and magnetic dyadic Green's functions, respectively, then they represent the solutions of the dyadic differential equations

$$\nabla \times \nabla \times \bar{\bar{G}}_{\mathrm{e}}(\bar{r}, \bar{r}') - k^2 \bar{\bar{G}}_{\mathrm{e}}(\bar{r}, \bar{r}') = \bar{\bar{I}}\delta(\bar{r} - \bar{r}'), \tag{4}$$

$$\nabla \times \nabla \times \bar{\bar{G}}_{\mathrm{m}}(\bar{r}, \bar{r}') - k^2 \bar{\bar{G}}_{\mathrm{m}}(\bar{r}, \bar{r}') = \nabla \times [\bar{\bar{I}}\delta(\bar{r} - \bar{r}')], \tag{5}$$

where $\bar{\bar{I}}$ denotes the idem factor and δ indicates the delta function. The integral solutions for (1) and (2) are given in [5,6].

The dyadic Green's function $\bar{\bar{G}}_{\mathrm{e}}(\bar{r}, \bar{r}')$ satisfying the Dirichlet boundary condition is called the electric dyadic Green's function of the first kind, and is denoted by $\bar{\bar{G}}_{\mathrm{e1}}(\bar{r}, \bar{r}')$. Then

$$\hat{n} \times \bar{\bar{G}}_{\mathrm{e1}}(\bar{r}, \bar{r}') = 0 \quad \text{on } S_1 \text{ and } S_2, \tag{6}$$

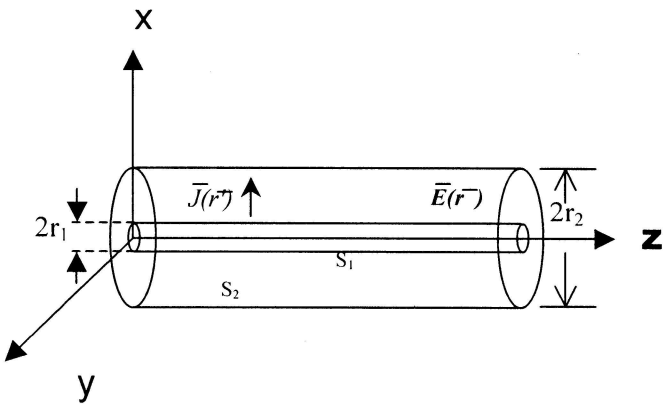

Figure 1. Co-axial line with a radially oriented current source located at $\bar{r}'$.

where $\hat{n}$ indicates the unit normal to the surface. The corresponding magnetic dyadic Green's function, designated as $\bar{\bar{G}}_{\mathrm{m2}}(\bar{r}, \bar{r}')$, is called the magnetic dyadic Green's function of the second kind. This function satisfies the Neumann boundary condition

$$\hat{n} \times \nabla \times \bar{\bar{G}}_{\mathrm{m2}}(\bar{r}, \bar{r}') = 0 \tag{7}$$

on the surfaces S_1 and S_2.

In order to find the electric field due to the current density, the eigenfunction expansions of $\bar{\bar{G}}_{\mathrm{e1}}(\bar{r}, \bar{r}')$ and $\bar{\bar{G}}_{\mathrm{m2}}(\bar{r}, \bar{r}')$ which satisfy the boundary conditions (6) and (7) at $r = r_1$ (inner conductor radius of the co-axial structure) and $r = r_2$ (outer conductor radius of the co-axial structure) are to be evaluated. The electric field due to $\bar{J}(\bar{r}')$ is then given by [5]

$$\bar{E}(\bar{r}) = -j\omega\mu_0 \iiint_v \bar{\bar{G}}_{\mathrm{e1}}(\bar{r}, \bar{r}') \cdot \bar{J}(\bar{r}')\mathrm{d}V'. \tag{8}$$

Equation (8), when evaluated for the TEM mode, takes its simplest form and gives the dominant mode electric field at the location $\bar{r}$. Techniques have been developed for computing the fundamental and harmonic components of this field due to multipactor current density, $\bar{J}(\bar{r}')$. With the assumption that the multipactor field is primarily a TEM field, an effort has been made to compare this field with the RF field that would be present in the co-axial line in the absence of multipactor. The dyadic Green's function (DGF) approach outlined above has the advantage that the same DGF is applicable for any arbitrary current distribution (linear, surface or volume), $\bar{J}(\bar{r}')$.

3. Evaluation of $\bar{\bar{G}}_{\mathrm{e1}}(\bar{r}, \bar{r}')$

The method of $\bar{\bar{G}}_{\mathrm{m}}$ is employed to derive an expression for $\bar{\bar{G}}_{\mathrm{e1}}(\bar{r}, \bar{r}')$. In this method, $\bar{\bar{G}}_{\mathrm{m2}}(\bar{r}, \bar{r}')$ is computed using the Ohm–Rayleigh method [7]

$$\bar{\bar{G}}^{\pm}_{\mathrm{m2}} = -j\pi\Bigg[c_{00}\bar{M}_{\mathrm{e}00}(\pm k)\bar{N}'_{\mathrm{e}00}(\mp k) + \sum_{n,\lambda}\frac{k}{k_\lambda}c_{n\lambda}\bar{M}_{\mathrm{e}_0 n\lambda}(\pm k_\lambda)\bar{N}'_{\mathrm{e}_0 n\lambda}(\mp k_\lambda) + \sum_{n,\mu}\frac{k}{k_\mu}c_{n\mu}\bar{N}_{\mathrm{e}_0 n\mu}(\pm k_\mu)\bar{M}'_{\mathrm{e}_0 n\mu}(\mp k_\mu)\Bigg] \quad \text{for} \quad \begin{matrix} z > z' \\ z < z' \end{matrix}, \tag{9}$$

where

$$c_{00} = \frac{1}{4\pi^2 I_0}, \quad c_{n\lambda} = \frac{2-\delta_0}{4\pi^2\lambda^2 I_\lambda}, \quad c_{n\mu} = \frac{2-\delta_0}{4\pi^2\mu^2 I_\mu},$$

$$\delta_0 = \begin{cases} 1, & n = 0 \\ 0, & n = 1 \end{cases}, \quad k_\lambda^2 = k^2 - \lambda^2, \quad k_\mu^2 = k^2 - \mu^2$$

$$\bar{M}_{\mathrm{e}00}(\pm k) = -\frac{\mathrm{e}^{\mp jkz}}{r}\hat{\phi}, \tag{10}$$

$$N'_{\mathrm{e}00}(\mp k) = \pm j\frac{k\mathrm{e}^{\pm jkz'}}{|k|r'}\hat{r}, \tag{11}$$

$$\bar{M}_{\mathrm{e}_0 n\lambda}(\pm k_\lambda) = \left[\mp\frac{nS_n(\lambda r)}{r}\begin{matrix}\sin\\\cos\end{matrix} n\phi\hat{r} - \frac{\partial S_n(\lambda r)}{\partial r}\begin{matrix}\cos\\\sin\end{matrix} n\phi\hat{\phi}\right]\mathrm{e}^{\mp jk_\lambda z}, \tag{12}$$

$$\bar{N}'_{\mathrm{e}_0 n\lambda}(\mp k_\lambda) = \frac{1}{k}\Bigg[\pm jk_\lambda\frac{\partial S_n(\lambda r)}{\partial r}\Big|_{r=r'}\begin{matrix}\cos\\\sin\end{matrix} n\phi'\hat{r} \mp\frac{jk_\lambda n}{r'}S_n(\lambda r')\begin{matrix}\sin\\\cos\end{matrix} n\phi'\hat{\phi} + \lambda^2 S_n(\lambda r')\begin{matrix}\cos\\\sin\end{matrix} n\phi'\hat{z}\Bigg]\mathrm{e}^{\pm jk_\lambda z'}, \tag{13}$$

$$\bar{N}_{\mathrm{e}_0 n\mu}(\pm k_\mu) = \frac{1}{k}\Bigg[\mp jk_\mu\frac{\partial T_n(\mu r)}{\partial r}\begin{matrix}\cos\\\sin\end{matrix} n\phi\hat{r} \pm\frac{jk_\mu n}{r}T_n(\mu r)\begin{matrix}\sin\\\cos\end{matrix} n\phi\hat{\phi} + \mu^2 T_n(\mu r)\begin{matrix}\cos\\\sin\end{matrix} n\phi\hat{z}\Bigg]\mathrm{e}^{\mp jk_\mu z}, \tag{14}$$

$$\bar{M}'_{\mathrm{e}_0 n\mu}(\mp k_\mu) = \left[\mp\frac{nT_n(\mu r')}{r'}\begin{matrix}\sin\\\cos\end{matrix} n\phi'\hat{r} - \frac{\partial T_n(\mu r)}{\partial r}\Big|_{r=r'}\begin{matrix}\cos\\\sin\end{matrix} n\phi'\hat{\phi}\right]\mathrm{e}^{\pm jk_\mu z'}, \tag{15}$$

where

$$S_n(\lambda r) = Y_n(\lambda r_1)J_n(\lambda r) - J_n(\lambda r_1)Y_n(\lambda r), \tag{16}$$

$$T_n(\mu r) = Y'_n(\mu r_1)J_n(\mu r) - J'_n(\mu r_1)Y_n(\mu r) \tag{17}$$

with

$$I_0 = \ln\left(\frac{r_2}{r_1}\right), \quad I_\lambda = \int_{r_1}^{r_2} S_n^2(\lambda r)\mathrm{d}r, \quad I_\mu = \int_{r_1}^{r_2} T_n^2(\mu r)\mathrm{d}r,$$
$$Y_n'(\mu r) = \frac{\partial Y_n(\mu r)}{\partial r}, \quad J_n'(\mu r) = \frac{\partial J_n(\mu r)}{\partial r}. \tag{18}$$

$\nabla \times \bar{\bar{G}}_{\mathrm{m2}}(\bar{r}, \bar{r}')$ is evaluated from eq. (9). This gives [5,6].

$$\begin{aligned}\nabla \times \bar{\bar{G}}^{\pm}_{\mathrm{m2}}(\bar{r}, \bar{r}') = -j\pi k^2 \Bigg[& \frac{1}{k} c_{00} \bar{N}_{\mathrm{e}00}(\pm k) \bar{N}'_{\mathrm{e}00}(\mp k) \\ & + \sum_{n,\lambda} \frac{1}{k_\lambda} c_{n\lambda} \bar{N}_{\mathrm{e}_0 n\lambda}(\pm k_\lambda) \bar{N}'_{\mathrm{e}_0 n\lambda}(\mp k_\lambda) \\ & + \sum_{n,\mu} \frac{1}{k_\mu} c_{n\mu} \bar{M}_{\mathrm{e}_0 n\mu}(\pm k_\mu) \bar{M}'_{\mathrm{e}_0 n\mu}(\mp k_\mu) \Bigg] \quad \text{for} \quad \begin{matrix} z > z' \\ z < z' \end{matrix}.\end{aligned} \tag{19}$$

Then according to the method of $\bar{\bar{G}}_{\mathrm{m}}$,

$$\bar{\bar{G}}_{\mathrm{e1}} = \frac{1}{k^2}[(\nabla \times \bar{\bar{G}}^{+}_{\mathrm{m2}})\, U^+ + (\nabla \times \bar{\bar{G}}^{-}_{\mathrm{m2}})\, U^- - \hat{z}\hat{z}\delta(\bar{r} - \bar{r}')], \tag{20}$$

where

$$U^+ = U(z - z') = \begin{cases} 1, & z > z' \\ 0, & z < z' \end{cases},$$
$$U^- = U(z' - z) = \begin{cases} 1, & z < z' \\ 0, & z > z' \end{cases}.$$

The argument $(\bar{r}, \bar{r}')$ has been omitted from eq. (20) onwards. Simplifying (20) gives

$$\bar{\bar{G}}^{+}_{\mathrm{e1}} = \frac{1}{k^2}\left[(\nabla \times \bar{\bar{G}}^{+}_{\mathrm{m2}}) - \hat{z}\hat{z}\delta\,(\bar{r} - \bar{r}')\right] \quad \text{for} \quad z > z', \tag{21}$$

$$\bar{\bar{G}}^{-}_{\mathrm{e1}} = \frac{1}{k^2}\left[(\nabla \times \bar{\bar{G}}^{-}_{\mathrm{m2}}) - \hat{z}\hat{z}\delta\,(\bar{r} - \bar{r}')\right] \quad \text{for} \quad z < z'. \tag{22}$$

In the above equations J_n and Y_n denote Bessel and Neumann functions of integral order respectively. The eigenvalues λ and μ are solutions of the characteristic equations

$$S_n(\lambda r_2) = Y_n(\lambda r_1) J_n(\lambda r_2) - J_n(\lambda r_1) Y_n(\lambda r_2) = 0 \tag{23}$$

and

$$T_n'(\mu r_2) = Y_n'(\mu r_1) J_n'(\mu r_2) - J_n'(\mu r_1) Y_n'(\mu r_2) = 0 \tag{24}$$

with

$$T_n'(\mu r) = \frac{\partial T_n(\mu r)}{\partial r}.$$

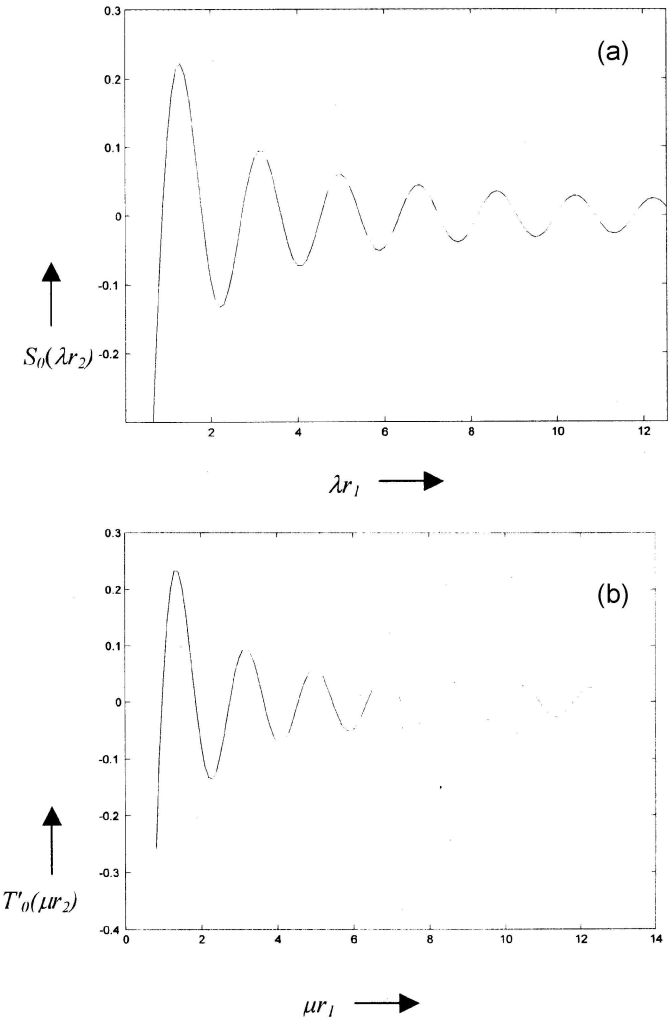

Figure 2. (**a**) Plot of S_0 (λr_2) vs. λr_1. (**b**) Plot of T'_0 (μr_2) vs. μr_1.

4. Computation of eigenvalues λ and μ

A code has been developed for computing λ and μ by directly evaluating the Bessel functions (J_n and J'_n) and Neumann functions (Y_n and Y'_n) over a range of argument where equations (23) and (24) are satisfied for a given order n. λ and μ are also calculated using the series given by Abramowitz and Stegun [8]. As the series given in [8] has only three terms, the accuracy suffers due to the truncation of series while computing the values of λ and μ. The direct computation method is precise and has distinct advantage over the latter method for higher order and lower values of the argument. Figures 2a and 2b show sample plots of $S_{(n=0)}(\lambda r_2)$ as against

λr_1 and $T'_{(n=0)}(\mu r_2)$ against μr_1. The dimensions of the TNC connector, which is normally used in communication payloads of the spacecraft, have been used in the computation. The zeroes of this $S_n(\lambda r_2)$ and $T'_n(\mu r_2)$ are then calculated and subsequently a set of λ, μ are calculated for a given order n. Tables 1 and 2 give the eigenvalues λ and μ computed by a direct solution of (23) and (24) and by employing the truncated series given in [8]. Tables 1a and 2a show, for the case when $n = 0$ in eq. (23), that the eigenvalues computed from the three term series given in [8] agree (to a great extent in table 1a and to a lesser extent in table 2a) with the values obtained using the numerical procedure described above. Tables 1b and 2b show that the three term series given in [8] is not adequate for computing the eigenvalues for the case when $n \neq 0$ in (23) and (24).

The accuracy of estimating the field of the higher order modes depends on the accuracy with which the eigenvalues λ and μ are determined.

Table 1a. Comparison of first twelve zeros calculated for $S_n(\lambda r_2)$ with $r_2 = 0.3035$ cm, $r_1 = 0.068$ cm and $n = 0$.

	Direct method		Series given in [8]	
Zero order	λr_1	λ (cm^{-1})	λr_1	λ (cm^{-1})
1	0.8845	13.0080	0.8218	12.0854
2	1.8006	26.4798	1.7920	26.3530
3	2.7117	39.8786	2.7090	39.8392
4	3.6211	53.2514	3.6199	53.2344
5	4.5296	66.6122	4.5290	66.6032
6	5.4377	79.9663	5.4373	79.9611
7	6.3455	93.3167	6.3453	93.3135
8	7.2532	106.6647	7.2530	106.6625
9	8.1607	120.0109	8.1606	120.0093
10	9.0682	133.3559	9.0681	133.3547
11	9.9756	146.7000	9.9755	146.6985
12	10.8830	160.0441	10.8829	160.0426

Table 1b. Comparison of first zero calculated for $S_n(\lambda r_2)$ with $r_2 = 0.3035$ cm, $r_1 = 0.068$ cm for $n = 0, 1, 2, 3$.

	Direct method		Series given in [8]	
Order n	λr_1	λ (cm^{-1})	λr_1	λ (cm^{-1})
0	0.8845	13.0080	0.8218	12.0854
1	0.9706	14.2737	1.09361	16.0825
2	1.1791	17.3410	0.8632	12.6954
3	1.4353	21.1087	−2.4813	−36.4902

Table 2a. Comparison of first twelve zeros calculated for $T'_n(\mu r_2)$ with $r_2 = 0.3035$ cm, $r_1 = 0.068$ cm and $n = 0$.

	Direct method		Series given in [8]	
Zero order	μr_1	μ (cm^{-1})	μr_1	μ (cm^{-1})
1	0.9706	14.2737	1.4743	21.6812
2	1.8544	27.2715	1.4745	21.6840
3	2.7501	40.4426	2.3252	34.1947
4	3.6506	53.6864	3.2138	47.2620
5	4.5536	66.9651	4.1116	60.4650
6	5.4578	80.2630	5.0130	73.7219
7	6.3629	93.5723	5.9164	87.0059
8	7.2684	106.8890	6.8207	100.3055
9	8.1743	120.2107	7.7258	113.6150
10	9.0804	133.5361	8.6313	126.9311
11	9.9867	146.8641	9.5371	140.2518
12	10.8931	160.1940	10.4431	153.5760

Table 2b. Comparison of the first zero calculated for $T'_n(\mu r_2)$ with $r_2 = 0.3035$ cm, $r_1 = 0.068$ cm for $n = 0, 1, 2, 3$.

	Direct method		Series given in [8]	
Order n	μr_1	μ (cm^{-1})	μr_1	μ (cm^{-1})
0	0.9706	14.2737	1.4743	21.6812
1	0.3756	5.5236	−1.2392	−18.2238
2	0.6775	9.9646	5.1028	75.0421
3	0.9403	13.8289	68.1486	1002.1864

5. Current source modelling

As explained earlier, when multipactor discharge takes place, the electrons move back and forth in the gap between the co-axial conductors. It has been assumed that the current element is oriented along the radial direction as shown in figure 3. The dipole is assumed to be located at $r' = r'_0$ and $\phi' = \phi'_0, z'_0 = 0$. Then

$$\begin{aligned}\bar{J}(\bar{r}')\mathrm{d}V' &= \frac{I(p\omega)}{r'_0 \mathrm{d}\phi' \mathrm{d}z'}\delta(r' - r'_0)\delta(\phi' - \phi'_0)\delta(z' - 0)\hat{r} \times r'_0\,\mathrm{d}\phi'\,\mathrm{d}z'\,\mathrm{d}r'_0 \\ &= I(p\omega)\mathrm{d}r'_0\delta(r' - r'_0)\delta(\phi' - \phi'_0)\delta(z' - 0)\hat{r}, \qquad (25)\end{aligned}$$

where p is the harmonic number and $I(p\omega)$ is the amplitude of the pth harmonic component of the multipactor current. Hence

$$\bar{\bar{G}}_{\mathrm{e1}} \cdot \bar{J}(\bar{r}')\mathrm{d}V' = \bar{\bar{G}}_{\mathrm{e1}} \cdot I(p\omega)\,\mathrm{d}r'_0\delta(r' - r'_0)\delta(\phi' - \phi'_0)\delta(z' - 0)\hat{r}. \qquad (26)$$

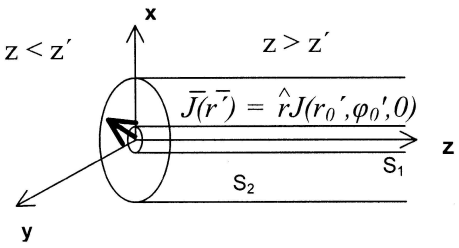

Figure 3. Multipactor current source in a co-axial geometry.

6. Evaluation of $\nabla \times \bar{\bar{G}}_{\mathbf{m2}}$

For $z > z'$, from eq. (19), $\nabla \times \bar{\bar{G}}^{+}_{\mathrm{m2}}$ is given by

$$\begin{aligned}(\nabla \times \bar{\bar{G}}^{+}_{\mathrm{m2}}) = &-j\pi k^2 \left[\frac{1}{k} c_{00} \bar{N}_{\mathrm{e}00}(k) \bar{N}'_{\mathrm{e}00}(-k)\right] \\ &-j\pi k^2 \left[\sum_{n,\lambda} \frac{1}{k_\lambda} c_{n\lambda} \bar{N}_{en\lambda}(k_\lambda) \bar{N}'_{en\lambda}(+k_\lambda)\right] \\ &-j\pi k^2 \left[\sum_{n,\mu} \frac{1}{k_\mu} c_{n\mu} \bar{M}_{en\mu}(k_\mu) \bar{M}'_{en\mu}(-k_\mu)\right]. \end{aligned} \tag{27}$$

Taking the dot product with $\hat{r}$,

$$\begin{aligned}(\nabla \times \bar{\bar{G}}^{+}_{\mathrm{m2}}) \cdot \hat{r} = \Bigg\{ &-j\pi k^2 \left[\frac{1}{k} c_{00} \bar{N}_{\mathrm{e}00}(k) \bar{N}'_{\mathrm{e}00}(-k)\right] \\ &-j\pi k^2 \left[\sum_{n,\lambda} \frac{1}{k_\lambda} c_{n\lambda} \bar{N}_{en\lambda}(k_\lambda) \bar{N}'_{en\lambda}(-k_\lambda)\right] \\ &-j\pi k^2 \left[\sum_{n,\mu} \frac{1}{k_\mu} c_{n\mu} \bar{M}_{en\mu}(k_\mu) \bar{M}'_{en\mu}(-k_\mu)\right]\Bigg\} \cdot \hat{r}. \end{aligned} \tag{28}$$

The first term in eq. (28) reduces to

$$-\frac{j}{4\pi I_0} k^2 \left[\frac{\mathrm{e}^{-jk(z-z')}}{rr'}\right].$$

The second term of eq. (28) reduces to

$$\begin{aligned}&\left[\sum_{n,\lambda} \left(\frac{2-\delta_0}{4\pi\lambda^2 I_\lambda}\right) \mathrm{e}^{-jk_\lambda(z-z')} \right. \\ &\quad \times \left(-jk_\lambda \frac{\partial S_n(\lambda r)}{\partial r} \cos n\phi \hat{r} + jk_\lambda n \frac{S_n(\lambda r)}{r} \sin n\phi \hat{\phi} \right. \\ &\quad \left. \left. + \lambda^2 S_n(\lambda r) \cos n\phi \hat{z}\right) \cdot \frac{\partial S_n(\lambda r)}{\partial r}\bigg|_{r=r'} \cos n\phi' \right]. \end{aligned}$$

Finally, the third term of eq. (28) reduces to

$$-jk^2 \sum_{n,\mu} \frac{1}{k_\mu} \left(\frac{2-\delta_0}{4\pi\mu^2 I_\mu} \right) \mathrm{e}^{-jk_\mu(z-z')} \times \left(\frac{nT_n(\mu r)}{r} \sin\, n\phi \hat{r} + \frac{\partial T_n(\mu r)}{\partial r} \cos\, n\phi \hat{\phi} \right) \times \left(\frac{nT_n\,(\mu r')}{r'} \sin\, n\phi' \right).$$

Evaluating the above three terms at the source coordinates, $(r'_0, \phi'_0, 0)$ leads to

$$\left(\nabla \times \bar{\bar{G}}^{+}_{\mathrm{m2}} \right) \cdot \hat{r} \Big|_{(r'_0,\phi'_0,0)} = \underbrace{-jk^2 \frac{\mathrm{e}^{-jkz}}{4\pi I_0 r r'_0} \hat{r}}_{\mathrm{TEM}} + \Bigg[\sum_{n,\lambda} \left(\frac{2-\delta_0}{4\pi\lambda^2 I_\lambda} \right) \mathrm{e}^{-jk_\lambda z} \times \left(-jk_\lambda \frac{\partial S_n(\lambda r)}{\partial r} \cos\, n\phi \hat{r} + j\frac{k_\lambda n}{r} S_n(\lambda r) \sin\, n\phi \hat{\phi} + \lambda^2 S_n(\lambda r) \cos\, n\phi \hat{z} \right) \times \left(\frac{\partial S_n(\lambda r)}{\partial r}\Big|_{r=r'=r'_0} \cos\, n\phi'_0 \right) \Bigg]_{\mathrm{TM}} - \Bigg[jk^2 \sum_{n,\mu} \left(\frac{2-\delta_0}{4\pi\mu^2 I_\mu} \right) \left(\frac{\mathrm{e}^{-jk_\mu z}}{k_\mu} \right) \times \left(\frac{nT_n(\mu r)}{r} \sin\, n\phi \hat{r} + \frac{\partial T_n(\mu r)}{\partial r} \cos\, n\phi \hat{\phi} \right) \left(\frac{nT_n(\mu r'_0)}{r'_0} \sin n\phi'_0 \right) \Bigg]_{\mathrm{TE}}. \quad (29)$$

The first term in eq. (29) corresponds to the TEM mode and the term in the square bracket corresponds to the higher order modes, TM and TE. Ignoring the higher order modes, the above equation reduces to

$$\left(\nabla \times \bar{\bar{G}}^{+}_{\mathrm{m2}} \right) \cdot \hat{r} \Big|_{(r'_0,\phi'_0,0)} = -jk^2 \frac{\mathrm{e}^{-jkz}}{4\pi I_0 r r'_0} \hat{r}. \quad (30)$$

Similarly, for $z < z'$, from eq. (19), $\nabla \times \bar{\bar{G}}^{-}_{\mathrm{m2}}$ is given by

$$\left(\nabla \times \bar{\bar{G}}^{-}_{\mathrm{m2}} \right) = -j\pi k^2 \left[\frac{1}{k} c_{00} \bar{N}_{\mathrm{e}00}(-k) \bar{N}'_{\mathrm{e}00}(+k) \right] - j\pi k^2 \left[\sum_{n,\lambda} \frac{1}{k_\lambda} c_{n\lambda} \bar{N}_{on\lambda}(-k_\lambda) \bar{N}'_{on\lambda}(+k_\lambda) \right] - j\pi k^2 \left[\sum_{n,\mu} \frac{1}{k_\mu} c_{n\mu} \bar{M}_{on\mu}(-k_\mu) \bar{M}'_{on\mu}(+k_\mu) \right].$$

Taking the dot product with $\hat{r}$, and evaluating the functions at the source coordinates

$$\left(\nabla \times \bar{\bar{G}}^{-}_{\mathrm{m2}} \right) \cdot \hat{r} \Big|_{(r'_0,\phi'_0,0)} = \underbrace{-jk^2 \frac{\mathrm{e}^{-jkz}}{4\pi I_0 r r'_0} \hat{r}}_{\mathrm{TEM}} - \Bigg[\sum_{n,\lambda} \left(\frac{2-\delta_0}{4\pi\lambda^2 I_\lambda} \right) \mathrm{e}^{jk_\lambda z}$$

$$\times\left(jk_\lambda\frac{\partial S_n(\lambda r)}{\partial r}\sin n\phi\hat{r}+\frac{jk_\lambda n}{r}S_n(\lambda r)\cos n\phi\hat{\phi}+\lambda^2 S_n(\lambda r)\sin n\phi\hat{z}\right)$$
$$\times\left(\left.\frac{\partial S_n(\lambda r)}{\partial r}\right|_{r=r'=r'_0}\sin n\phi'_0\right)\Bigg]_{\mathrm{TM}}-\Bigg[jk^2\sum_{n,\mu}\frac{2-\delta_0}{4\pi\mu^2 I_\mu}\ \frac{\mathrm{e}^{-jk_\mu z}}{k_\mu}$$
$$\times\left(\frac{nT_n(\mu r)}{r}\cos n\phi\hat{r}-\frac{\partial T_n(\mu r)}{\partial r}\sin n\phi\hat{\phi}\right)\left(\frac{nT_n(\mu r'_0)}{r'_0}\cos n\phi'_0\right)\Bigg]_{\mathrm{TE}}. \quad (31)$$

Ignoring higher order modes in eq. (31), the TEM mode is given by

$$\left(\nabla\times\bar{\bar{G}}^-_{\mathrm{m2}}\right)\cdot\hat{r}\Big|_{(r'_0,\phi'_0,0)}=-jk^2\frac{\mathrm{e}^{jkz}}{4\pi I_0 r r'_0}\hat{r}. \quad (32)$$

From eqs (21) and (30) it may be shown that

$$\bar{\bar{G}}^+_{\mathrm{e1}}\cdot\hat{r}\Big|_{(r'_0,\phi'_0,0)}=\frac{1}{k^2}(\nabla\times\bar{\bar{G}}^+_{\mathrm{m2}})\cdot\hat{r}\Big|_{(r'_0,\phi'_0,0)}$$
$$=-j\frac{\mathrm{e}^{-jkz}}{4\pi I_0 r r'_0}\hat{r},\quad z>z'. \quad (33)$$

Substituting eqs (26) and (33) in (8), the electric field (TEM mode) for $z>z'$, is given by

$$\bar{E}^+(\bar{r})=-jp\omega\mu_0 I(p\omega)\int_{r_1}^{r_2}\frac{-j\mathrm{e}^{-jkz}}{4\pi k I_0 r r'_0}\hat{r}\mathrm{d}r'_0$$
$$=\frac{-p\omega\mu_0 I(p\omega)\mathrm{e}^{-jkz}}{4\pi kr}\hat{r},\quad z>z'. \quad (34)$$

Similarly, from eqs (22) and (32) it may be shown that

$$\bar{\bar{G}}^-_{\mathrm{e1}}\cdot\hat{r}\Big|_{(r'_0,\phi'_0,0)}=\frac{1}{k^2}(\nabla\times\bar{\bar{G}}^-_{\mathrm{m2}})\cdot\hat{r}\Big|_{(r'_0,\phi'_0,0)},\quad z<z'$$
$$=-j\frac{\mathrm{e}^{jkz}}{4\pi I_0 r r'_0}\hat{r}. \quad (35)$$

Therefore the electric field (TEM mode) for $z<z'$ is given by

$$\bar{E}^-(\bar{r})=-jp\omega\mu_0 I(p\omega)\int_{r_1}^{r_2}\frac{-j\mathrm{e}^{jkz}}{4\pi I_0 k r r'_0}\hat{r}\mathrm{d}r'_0$$
$$=\frac{-p\omega\mu_0 I(p\omega)\mathrm{e}^{jkz}}{4\pi kr}\hat{r},\quad z<z'. \quad (36)$$

Thus, from eqs (34) and (36), it may be observed that the magnitudes of the electric field remain the same along the z-direction. For the current source located at $z'=0$, the two equations represent waves propagating away from the source.

In the absence of multipactor, the E-field of the TEM mode in the co-axial line is given by

$$\bar{E}_{\mathrm{RF}}(\bar{r}) = -\hat{r}\frac{V_0}{r\ln(r_2/r_1)}\mathrm{e}^{j(\omega t-kz)}$$
$$= -\hat{r}\frac{(2PZ_0)^{1/2}}{rI_0}\mathrm{e}^{j(\omega t-kz)}, \quad \text{for} \quad z > z', \tag{37}$$

where V_0 is the amplitude of RF voltage, P is the RF power in the co-axial line and Z_0 is the characteristic impedance of the co-axial line.

The magnitude of the ratio of fields given by eqs (34), (36) and (37) is

$$\left|\frac{\bar{E}^{\pm}(\bar{r})}{\bar{E}_{\mathrm{RF}}(\bar{r})}\right| = \frac{p\omega\mu_0 I_0 I(p\omega)}{4\pi\, k\sqrt{(2PZ_0)}}, \tag{38}$$

wherein $\bar{E}^{\pm}(\bar{r})$ represents $\bar{E}^{+}(\bar{r})$ for $z > z'$ and $\bar{E}^{-}(\bar{r})$ for $z < z'$.

7. Higher order modes

In eqs (29) and (31), the higher order modes, TM and TE, are represented by the terms given in the square brackets. The cut-off frequencies of these modes can be calculated using the λ and μ values given in tables 1b and 2b, by setting the following conditions: $k_\lambda^2 = k_{\mathrm{c}}^2 - \lambda^2 = 0$ and $k_\mu^2 = k_{\mathrm{c}}^2 - \mu^2 = 0$, where $k_{\mathrm{c}}^2 = 2\pi/\lambda_{\mathrm{c}}$, and λ_{c} is the cut-off wavelength.

The values are compared with the approximate solutions of the cut-off frequency, $f_{\mathrm{c}} = c/\lambda_{\mathrm{c}}$, given in [9]. Adopting the usual conventions for mode representation, the cut-off frequency, for the different modes are approximately given by

$$\mathrm{TM}_{nm}\ \text{modes} : f_{\mathrm{c}} \cong \frac{mc}{2(r_2 - r_1)}, \tag{39}$$

$$\mathrm{TE}_{n1}\ \text{modes} : f_{\mathrm{c}} \cong \frac{nc}{2(r_2 + r_1)}, \tag{40}$$

$$\mathrm{TE}_{nm}\ \text{modes}\ (m \geq 2) : f_{\mathrm{c}} \cong \frac{(m-1)c}{2(r_2 + r_1)}, \tag{41}$$

where the velocity of light is denoted by c. The results are compared in table 3. As a special case, the first higher order mode TE_{11} cut-off frequency is also computed by transverse resonance technique [10]. As per this technique the cut-off wavelength, λ_{c} is given by

$$\lambda_{\mathrm{c}} = 2\pi r_{\mathrm{m}}\left[1 - \frac{1}{6}\left(\frac{d}{2r_{\mathrm{m}}}\right)^2 - \frac{7}{120}\left(\frac{d}{2r_{\mathrm{m}}}\right)^4 - \cdots\right], \tag{42}$$

where $d = r_2 - r_1$, $r_{\mathrm{m}} = (r_2 + r_1)/2$.

Substituting the values in eq. (42) the cut-off frequency for TE_{11} mode is 27.8308 GHz. Referring to table 2b for TE_{11} mode, $\mu = 5.523621\ \mathrm{cm}^{-1}$ and the cut-off

Table 3. Comparison of higher order modes in co-axial geometry using the eigenvalues and eqs (39)–(41) [9] ($r_2 = 0.3035$ cm, $r_1 = 0.068$ cm).

Modes	λ (cm^{-1})	μ (cm^{-1})	Cut-off frequency (in GHz)	
			Using eigenvalues λ, μ	Using eqs (39)–(41)
TE_{11}	–	5.52361	26.373295	25.704701
TE_{21}	–	9.96464	47.577651	51.409402
TM_{01}	13.00805	–	62.108863	63.694267
TE_{31}	–	13.82897	66.028468	77.114104
TM_{11}	14.27379	–	68.152327	63.694267
TM_{02}	26.47985	–	126.4319706	127.388535

frequency will be 26.3733 GHz which very closely matches the value of 25.7047 GHz calculated using eq. (40). As the cut-off frequency for the TE_{11} mode is determined by solving the characteristic equation directly, the frequency value given by this method would be more accurate. Moreover, the eigenvalues λ and μ are useful in carrying out the evolution of TE and TM fields by employing eq. (31).

The estimation of the strength of TE_{11} mode and how it decays with distance from the source for $z > z'$ and $z < z'$ is important to know its contribution to the noise while multipactor occurs. From eqs (29) and (31) and from table 2b, the propagation factor for the fundamental frequency can be easily shown to be $e^{-5.2293z}$ (for $z > z'$) and $e^{5.2293z}$ (for $z < z'$). Thus at $z = 1$ cm, from the source the TE_{11} mode attenuates by about 45 dB.

8. Results of numerical computation

Computer simulation of multipactor in co-axial geometry has been carried out to compute the ratio of the electric field with and without the multipactor in the co-axial gap. The harmonics $I(p\omega)$ of multipactor current have been computed and then substituted in eq. (38). A typical case of TNC connector has been taken for this computer simulation exercise. The inputs to the program are as follows:

- Co-axial dimensions $r_1 = 0.068$ cm; $r_2 = 0.3035$ cm (TNC interface: MIL-C-87104/2).
- Initial velocity of the electron $= 1.3 \times 10^6$ m/s.
- Frequency $\times$ distance $(Fd) = 200$ MHz-cm.
- Multipactor mode $= 1$.
- During the steady state multipactor, it is assumed that the number of electrons involved reaches a saturation state and there will not be any further increase in the population of electrons. The studies have shown that the amount of the RF power dissipated due to the multipactor lies over a wide range of 1% to 50%. The percentage of dissipation depends on the strength of the multipactor current or in other words, the number of electrons involved in

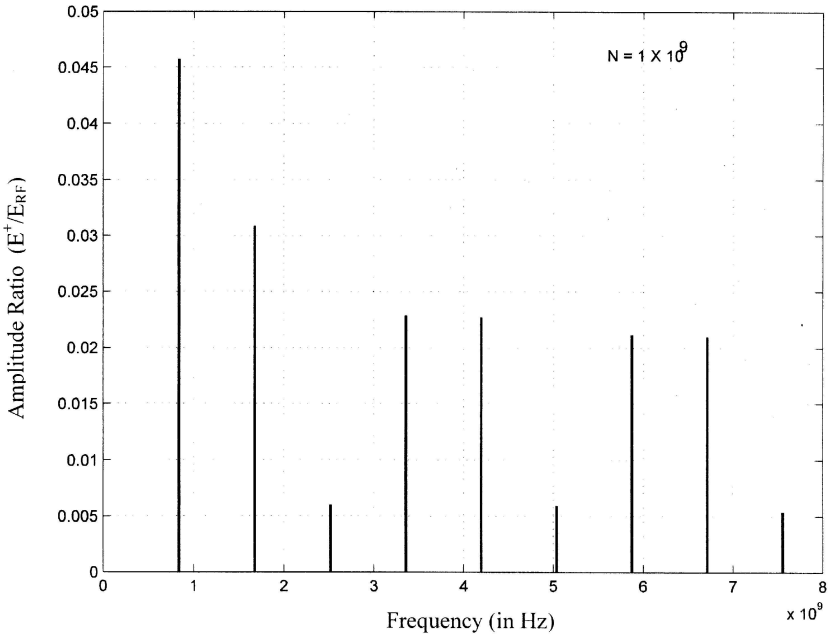

Figure 4. Harmonic spectrum of the magnitude of field ratio for $N = 10^9$.

multipactor. Studies [11] have shown that power dissipation of 9% is possible when the number of electrons, N, in the multipactor is around 10^9.

The results of the field harmonic computations are shown in figure 4 and the amplitudes ratios have been tabulated in table 4. The fundamental RF frequency for frequency $\times$ distance (Fd) = 200 MHz-cm is 849.26 MHz. The second harmonic amplitude is about -3.4 dB below the fundamental component of the radiated field. Hence this harmonic is about -30 dB below the fundamental component of the RF field in the co-axial line. This can pose problems in a high power communication satellite wherein high power transmitters and sensitive receivers (receiver sensitivity <-90 dBm) are co-located on the spacecraft platform. Even if a cross-polarization isolation of 30 dB and other isolations are considered, any harmonic falling within the receiver bandwidth can easily be a source of interference. The interference problem would be still more severe if a common antenna is employed for transmission and reception.

9. Conclusion

The dyadic Green's function technique has been employed for computing the radiated electric field due to multipactor current in a coaxial geometry. The field in the absence of the multipactor is compared with the field radiated due to multipactor. The results indicate that distortion in the RF field within the gap due to multipactor does occur. The strength of the second harmonic component of the

Table 4. Amplitude ratios of the field harmonics ($N = 1 \times 10^9$).

Harmonic number	Frequency (in GHz)	Amplitude ratio (E^+/E_{RF})	(in −dB)
1	0.839	0.0457	−26.8017
2	1.678	0.0308	−30.2290
3	2.517	0.0059	−44.5830
4	3.357	0.0228	−32.8413
5	4.196	0.0227	−32.8795
6	5.035	0.0059	−44.5830
7	5.875	0.0211	−33.5144
8	6.714	0.0209	−33.5971
9	7.553	0.0054	−45.3521
10	8.393	0.0210	−33.5556
11	9.232	0.0204	−33.8074
12	10.072	0.0047	−46.5580
13	10.911	0.0208	−33.6387
14	11.750	0.0204	−33.8074
15	12.589	0.0457	−26.8017

radiated field due to multipactor current element will be small (about −30 dB for $N = 10^9$) in comparison with field due to RF carrier field strength in the absence of multipactor. The component can pose problems in a communication satellite wherein high power transmitters and sensitive receivers (receiver sensitivity <-90 dBm) are co-located on the spacecraft platform. The higher order modes in co-axial geometry have been determined accurately by solving the characteristic equations. The cut-off frequencies (of higher order modes) computed from other methods and the method outlined in this paper have been compared. The higher order modes contribute to system noise and hence a theoretical investigation of their levels would be useful in noise level prediction.

References

[1] *The study of multipactor breakdown in space electronic systems*, NASA-CR-488, Hughes Aircraft Co., July 1966
[2] R Woo, *J. Appl. Phys.* **39(3)**, 1528 (1968)
[3] R Woo, *Final report on RF voltage breakdown in coaxial transmission lines*, NASA-TR 32-500, October 1970
[4] S V K Shastry *et al*, *Multipactor breakdown in spacecraft microwave systems*, Doc. No. ISRO-ISAC-TR-0335, November 1998
[5] Tai Chen-To, *Dyadic green functions in electromagnetic theory* (IEEE Press, Piscataway, NJ, 1994)
[6] Tai Chen-To, *IEEE Trans. Ant Prop.* **31(2)**, 355 (1983)
[7] A Sommerfeld, *Partial differential equations* (Academic Press, New York, 1949)

[8] M Abramowitz and I A Stegun, *Handbook of mathemetical functions bureau of standards* (US Government Printing Office, Washington DC, 1964)
[9] S R Pennock and P R Shepherd, *Microwave engineering with wireless applications* ISBN: 0070497222 (McGraw-Hill, 1998)
[10] H E Green, *IEEE Trans. Microwave Theory and Technique* **37(10)**, 1652 (1989)
[11] S K Nagesh, S V K Shastry and L Revannasiddiah, *J. Spacecraft Technol.* **14(2)**, 19 (2004)